Surfaces and Interfaces 61 (2025) 106094

Contents lists available at ScienceDirect

Surfaces and Interfaces

journal homepage: www.sciencedirect.com/journal/surfaces-and-interfaces

Interfacial engineering with a monobromo-carbazole-based molecular modifier for a robust PTAA/perovskite heterointerface

Uijoon Lee [a,b,1], Min Kyoung Shin [c,1], Heejun Lee [d,1], Byungsoo Kang [a,e], Minseok Kim [a], Sooyoung Han [c], Taehee Kim [a], Hae Jung Son [a], Phillip Lee [a,e], Rongrong Cheacharoen [f], Dong Hoe Kim [b], Joonho Bang [d,g,*], Jongin Hong [c,h,**], Yoon Hee Jang [a,***]

[a] Advanced Photovoltaics Research Center, Korea Institute of Science and Technology (KIST), Seoul 02792, Republic of Korea
[b] Department of Materials Science and Engineering, Korea University, Seoul, 02841, Republic of Korea
[c] Department of Chemistry, Chung-Ang University, Seoul 06974, Republic of Korea
[d] Department of Materials Engineering and Convergence Technology, Gyeongsang National University, Jinju 52828, Republic of Korea
[e] Division of Nano and Information Technology, KIST School, University of Science and Technology, Seoul 02792, Republic of Korea
[f] Metallurgy and Materials Science Research Institute, Chulalongkorn University, Bangkok 10330, Thailand
[g] School of Materials Science and Engineering, Gyeongsang National University, Jinju 52828, Republic of Korea
[h] Department of Smart Cities, Chung-Ang University, Seoul 06974, Republic of Korea

ARTICLE INFO

Keywords:
Perovskite solar cell
Hole transport layer
Self-assembled monolayer
PTAA
$MAPbI_3$

ABSTRACT

The fine-tuning of the interfacial properties between the hole transport layer (HTL) and the active perovskite layer is important to achieve high efficiency in inverted perovskite solar cells (PSCs). Interfacial layers are crucial in aligning energy levels and mitigating defect-induced losses, thereby facilitating charge transfer and device stability. This study introduces an advanced interfacial engineering technique via utilization of an asymmetric monobromo-substituted carbazole-based molecular modifier, [4-(3-bromo-9H-carbazol-9-yl)butyl]phosphonic acid (3Br-Cz-4PA), to improve the compatibility between the underlying HTL of poly[bis(4-phenyl)(2,4,6-trimethylphenyl)amine] (PTAA) and the perovskite layer of methylammonium lead iodide ($MAPbI_3$). Through the integrated density functional theory calculations and empirical studies, it is revealed that 3Br-Cz-4PA not only passivates undercoordinated Pb defects but also facilitates hole extraction by suppressing non-radiative recombination. Moreover, this approach yields a notable improvement in the grain growth and crystallinity of perovskite films. Consequently, PSCs enhanced with 3Br-Cz-4PA demonstrate a remarkable power conversion efficiency of 19.3 %, minimal hysteresis, and superior shelf-life stability, positioning this methodology as a substantial leap forward photovoltaic technology.

1. Introduction

Organic-inorganic halide perovskite solar cells (PSCs) have achieved impressive power conversion efficiencies (PCEs), reaching 26.7 %, which closely rivals that of crystalline silicon (Si) solar cells at 27.1 % [1]. The rapid advancement in PSC efficiency, along with their cost-effective fabrication and versatile design options, position them as leading contenders in the next-generation photovoltaic technologies. Notably, the inverted (p-i-n) configuration has gained commercial prominence due to its enhanced operational reliability, scalability, and compatibility with various tandem device architecture [2–7]. Despite historically lagging behind the performance of standard (n-i-p) configurations, recent breakthroughs have propelled p-i-n PSCs exceed the 25 % efficiency mark [8–10]. Recently, the PCE of p-i-n PSCs surpassed the record performance of n-i-p devices [11,12]. Significant improvements have been driven by advancements in the hole transport layer (HTL) and strategies aimed at reducing energy losses at the HTL/perovskite interface [13–17]. Selecting appropriate HTL materials is crucial

* Corresponding author at: Department of Materials Engineering and Convergence Technology, Gyeongsang National University, Jinju 52828, Republic of Korea.
** Corresponding author at: Department of Chemistry, Chung-Ang University, Seoul 06974, Republic of Korea.
*** Corresponding author at: Advanced Photovoltaics Research Center, Korea Institute of Science and Technology (KIST), Seoul 02792, Republic of Korea.
E-mail addresses: bang@gnu.ac.kr (J. Bang), hongj@cau.ac.kr (J. Hong), yhjang@kist.re.kr (Y.H. Jang).
[1] These authors contributed equally to this work.

https://doi.org/10.1016/j.surfin.2025.106094
Received 29 July 2024; Received in revised form 9 February 2025; Accepted 21 February 2025
Available online 22 February 2025

for optimizing the performance of p-i-n PSCs, influencing key aspects such as charge carrier extraction, recombination rates, and overall device stability. Various materials, including poly(3,4-ethylenedioxythiophene):poly(styrenesulfonate) (PEDOT:PSS), self-assembled monolayers (SAMs), inorganic p-type metal oxides like NiO_x, and poly[bis(4-phenyl)-(2,4,6,-trimethylphenyl)amine] (PTAA), have demonstrated effectiveness as HTLs [18–21]. PTAA, in particular, is noted for its superior electrical properties and structural advantages [21–23]. However, the hydrophobic nature of PTAA, while boosting device stability [24,25], reduces the wettability of the perovskite solution, leading to poorer quality films and energy losses due to inadequate interfacial contact [26,27].

Addressing this challenge, interface engineering has emerged as a pivotal strategy for optimizing the interaction between PTAA and perovskite layers [28–34]. This approach focuses on tailoring properties such as hole transport, surface energy, and contact affinity at the PTAA interface to improve charge extraction and minimize charge carrier loss. Effective interface engineering not only enhances the HTL properties but also benefits the perovskite layer by improving crystallinity and passivating defects. Innovations in materials and modifiers for interface engineering adjust HTL surface properties to facilitate charge transport. SAM molecules, for example, are widely used for HTL modification, effectively fine-tuning interfacial properties [35–39]. These molecules typically consist of a substrate-anchoring head group, an alkyl tail, and a functional end group, each playing a unique role in the assembly and substrate interaction [40]. The design of SAMs is customizable, allowing for precise adjustments of interfacial characteristics between the HTL and perovskite layers [41]. The properties of the functional end group, particularly its chemical nature and electronic characteristics, are vital for forming ultrathin, charge-selective contacts in PSCs [36,42,43]. For instance, Wang *et al.* [36] demonstrated that 4-bromobenzoic acid SAMs on NiO_x HTL significantly enhanced both photovoltaic performance and stability. Thus, the molecular design of SAMs is crucial in optimizing energy levels and surface properties, suppressing defect formation and recombination losses, thereby enhancing overall PSC performance and stability. Studies have shown that halogen-substituted SAM molecules markedly improve hole extraction [44–47]. By varying the chemical substitutions in SAMs, key properties such as wettability, dipole moments, and surface potential can be tuned, influencing overall device performance [46–49].

Inspired by these insights, our study introduces a novel monobromo-carbazole-based SAM molecule, specifically (4-(3-bromo-9H-carbazol-9-yl)butyl)phosphonic acid (3Br-Cz-4PA), for use in p-i-n PSCs. We successfully incorporated 3Br-Cz-4PA at the PTAA/perovskite interface, significantly enhancing perovskite grain growth through tailored surface properties of PTAA, while also effectively passivating undercoordinated Pb^{2+} defects at the PTAA/perovskite heterointerface to complete the octahedral coordination of PbX_6. Density functional theory (DFT) calculations further confirmed the effectiveness of this approach in passivating undercoordinated surface Pb cations and establishing robust chemical interactions between 3Br-Cz-4PA and the perovskite. This modification not only promoted efficient hole transfer but also reduced non-radiative recombination due to favorable energy level alignment at the interface. Consequently, methylammonium lead iodide ($MAPbI_3$)-based PSCs incorporating 3Br-Cz-4PA achieved a PCE of 19.3 %. Remarkably, these devices retained over 95 % of their initial efficiency even after 30 days of exposure to ambient conditions without encapsulation. This underscores the potential of the asymmetric monobromo-SAM material to significantly enhance both the efficiency and stability of PSCs.

2. Material and methods

2.1. Materials

Methylammonium iodide (MAI, >99.99 %) was sourced from Greatcell Solar Materials. Lead(II) iodide (PbI_2, 99.99 %, trace metal basis) and bathocuproine (BCP, 98 %) were procured from TCI and Alfa Aesar, respectively. Poly(triaryl amine) (PTAA, >99.9 %, trace metal basis) was obtained from 1-Materials Inc. [6,6]-phenyl-C61-butyric acid methyl ester ($PC_{61}BM$, >99.5 %) was supplied by Brillant Materials. Anhydrous solvents including ethyl alcohol (EtOH, anhydrous, ≥99.5 %), chlorobenzene (CB, anhydrous, 99.8 %), toluene (anhydrous, 99.8 %), isopropyl alcohol (IPA, anhydrous, 99.5 %), N,N-dimethylformamide (DMF, anhydrous, 99.8 %), dimethyl sulfoxide (DMSO, anhydrous, >99.9 %), and ethyl acetate (EA, anhydrous, 99.8 %), were purchased from Sigma-Aldrich. Acetone, EtOH, and IPA used for substrate cleaning were supplied by Daejung Chemicals & Metals Co., Ltd.

2.2. Solar cell fabrication

PSCs were constructed with a p-i-n structure: ITO/PTAA/$MAPbI_3$/$PC_{61}BM$/BCP/Ag. Indium tin oxide (ITO) coated glass substrates (150 nm-thick, ~9 Ω/sq., dimensions 24.5 mm × 24.5 mm) were sequentially cleaned in an ultrasonic bath with acetone, EtOH, and IPA for 10 min each. Then, substrates were dried under a stream of nitrogen and stored in a dry oven. Prior to fabrication, ITO substrates were subjected to UV-ozone treatment for 20 min and moved to a N_2-filled glove box. A toluene solution of PTAA (1.5 mg mL^{-1}) was spin-coated on the ITO at 2000 rpm for 40 s (acceleration 1000 rpm s^{-1}) and annealed at 100 °C for 10 min. For the control group, PTAA films were subjected to a DMF prewash at 4000 rpm for 30 s. For the experimental group, 3Br-Cz-4PA dissolved in ethanol was spin-coated onto PTAA films at 3000 rpm for 30 s, annealed 100 °C for 10 min, followed by an ethanol wash. The perovskite precursor (MAI, PbI_2, DMSO in DMF) was stirred overnight, filtered through a 0.45 μm PTFE filter, and 100 μL was spin-coated onto the prepared PTAA films at 8000 rpm for 20 s. Just prior to the end of this process, 70 μL of EA was dropped onto the spinning substrates as an anti-solvent. The resultant films were annealed at 65 °C for 1 min, then 100 °C for 10 min. A CB solution of $PC_{61}BM$ (20 mg mL^{-1}) was spin-coated over the perovskite at 2000 rpm for 30 s and annealed at 100 °C for 10 min. Subsequently, an IPA solution of BCP (1.5 mg mL^{-1}) was deposited on the $PC_{61}BM$ layer at 4000 rpm for 40 s. The cell assembly was completed with the thermal evaporation of a 100 nm-thick Ag electrode at 2 Å s^{-1}, with a shadow mask defining the active area of 0.09 cm^2.

2.3. Characterization of films and devices

Current density-voltage ($j-V$) characteristics were measured under AM 1.5G illumination (100 mW cm^{-2}) using a class AAA solar simulator (YSS-50A, Yamashita Denso) equipped with a 180 W Xe lamp and a Keithley 2400 source meter. Intensity calibration was performed using a Si reference cell, calibrated by the National Renewable Energy Laboratory (NREL), fitted with a KG-5 filter (PV Measurements, Inc.). $j-V$ curves were recorded in both backward and forward scan modes with a 100 ms delay between data points. External quantum efficiencies (EQEs) were determined with a Quantum Efficiency Measurement Solution (QuantX-300, Newport) using intensity-calibrated monochromated light from a Xe arc lamp. A patented Newport Si/Ge detector measured the EQE spectra. Field-emission scanning electron microscopy (FE-SEM, Inspect F, FEI) at 10 keV visualized surface morphology, while a 7 keV setting imaged device cross-sections. The topography of PTAA films was assessed with atomic force microscopy (AFM, XE-100, Park Systems). X-ray diffraction (XRD, Rigaku Dmax2500/PC) with Cu Kα radiation (λ = 1.5406 Å) scanned perovskite films in grazing incidence mode at 2°/min. Optical properties were probed with a Lambda 365 ultraviolet-visible (UV–Vis) spectrophotometer (PerkinElmer), and steady-state photoluminescence (PL) spectra came from a FP-8500 spectrofluorometer (JASCO) at 530 nm excitation. X-ray photoemission spectroscopy (XPS, Thermo Scientific Nexsa system) utilized a microfocus

monochromated Al Kα source, and ultraviolet photoemission spectroscopy (UPS) measurements were conducted with a He I discharge lamp ($h\nu = 21.22$ eV), with pass energies of 1.0 eV for work function and 5.0 eV for valence band measurements. Contact angle (CA) measurements were performed using a PCA-1 contact angle meter (Kyowa Interface Science) and documented using FAMAS software (V 3.2.2) under ambient conditions.

2.4. Synthesis of 3Br-Cz-4PA

All chemicals and solvents were purchased from Sigma-Aldrich and used as received without purification. 3-bromo-9-(4-bromobutyl)-9H-carbazole (1), diethyl(4-(3-bromo-9H-carbazol-9-yl)butyl)phosphate (2), [4-(3-bromo-9H-carbazol-9-yl)butyl]phosphonic acid (3) were synthesized according to the scheme shown in Scheme S1. The ^{1}H and ^{13}C nuclear magnetic resonance (NMR) spectra, along with the high-resolution electrospray ionization mass spectrometry (ESI-HRMS) spectrum of the final product, are provided in Figs. S1 and S2.

3-bromo-9-(4-bromobutyl)-9H-carbazole (1): 3-bromo-9H-carbazole (2 g, 8.13 mmol) and powdered anhydrous potassium carbonate (5.53 g, 40.05 mmol) were dissolved in anhydrous acetonitrile (32 mL). 1,4-dibromobutane (9.70 mL, 81.26 mmol) was then added. The reaction vessel was flushed with N_2, maintaining this atmosphere throughout the reaction. The mixture was stirred and refluxed in an oil bath at 95 °C for 48 h. After cooling, the mixture was filtered, and the solvent evaporated to yield a solid. This solid was recrystallized from petroleum ether, producing 2.26 g (73 %) of compound 1. ^{1}H NMR (300 MHz, $CDCl_3$) δ: 8.18 (s, 1H), 8.03 (d, J = 15 Hz, 1H), 7.50 (m, 2H), 7.38 (d, J = 9 Hz, 1H), 7.24 (t, J = 6 Hz, 2H), 4.30 (m, 2H), 3.36 (t, J = 4 Hz, 2H), 2.07–1.83 ppm (m, 4H).

Diethyl(4-(3-bromo-9H-carbazol-9-yl)butyl)phosphonate (2): Compound 1 (1 g, 2.62 mmol) was dissolved in triethylphosphite (9.45 mL). The mixture was refluxed at 165 °C for 20 h, and then the solvent was removed under reduced pressure. The crude product underwent column chromatography, starting with n-hexane and gradually shifting to an acetone/hexane mixture (1/4, v/v). This process yielded 1.15 g (100 %) of a clear liquid that crystallized into compound 2. ^{1}H NMR (300 MHz, $CDCl_3$) δ: 8.10 (d, J = 1.9 Hz, 2H), 8.03 (d, J = 15 Hz, 1H), 7.56 (dd, J = 8.7, 1.8 Hz, 2H), 7.30 (d, J = 8.7 Hz, 2H), 4.60–4.48 (m, 2H), 4.03 (q, J = 7.3 Hz, 4H), 2.29–2.17 (m, 2H), 1.23 ppm (t, J = 7.1 Hz, 6H)

(4-(3-bromo-9H-carbazol-9-yl)butyl)phosphonic acid, 3Br-Cz-4PA (3): Compound 2 (1.2 g, 2.74 mmol) was dissolved in dry 1,4-dioxane (26 mL) under an N_2 atmosphere. Bromotrimethysilane (3.80 mL) was added dropwise. The reaction proceeded for 24 h at 25 °C under N_2. Methanol (24 mL) was then introduced, and the solvent reduced under pressure until a minimal volume remained. Distilled water was added dropwise to precipitate the product. The resultant solid was filtered and washed with water, yielding 0.74 g (71 %) of 3Br-Cz-4PA as a white solid. ^{1}H NMR (600 MHz, MeOD) δ: 8.16 (d, J = 2 Hz, 1H), 8.02 (d, J = 6 Hz, 1H), 7.49−7.42 (m, 3H), 7.39 (d, J = 6 Hz, 1H) 7.18 (t, J = 6 Hz, 1H), 4.31 (t, J = 6 Hz, 2H), 1.95−1.90 (m, 2H), 1.71–1.60 ppm (m, 4H); ^{13}C NMR (151 MHz, MeOD) δ: 140.66, 138.95, 127.83, 126.13, 124.44, 122.36, 121.60, 119.99, 118.91, 111.05, 110.21, 108.80, 48.02, 47.88, 47.73, 47.59, 47.45, 47.31, 47.17, 42.05, 29.52, 29.41, 26.85, 25.93, 20.32, 20.28. (ESI-HRMS) Calcd for $C_{16}H_{16}BrNO_3P$ $[M\text{-}H]^-$ 380.0051, Found: 380.0052.

2.5. Density functional theory (DFT) calculations

Computational analyses of SAM molecules were conducted using the Gaussian 09 program [50]. For DFT calculations, geometry optimizations were carried out with the B3LYP functional and the 6–31G(d,p) basis set. All optimized structures were verified as local minima on their respective potential energy surfaces, confirmed by the absence of imaginary frequencies in their vibrational frequencies. To account for solvation effects and improve the accuracy of solvation energy predictions the solvation model density (SMD) was employed [51]. After optimization, dipole moment vectors were calculated to evaluate the direction and magnitude of intrinsic polarity in a molecule. The electrostatic potential (ESP) maps were generated to visualize the surface charge distribution of each molecule.

To further explore the interaction between the perovskite and PTAA (or 3Br-Cz-4PA) layers, computational analyses were executed utilizing the projector-augmented-wave method [52] combined with the Perdew–Burke–Ernzerhof generalized gradient approximation [53], as implemented in the Vienna Ab initio Simulation Program (VASP) code [54]. The following valence electron configurations were used: H (1s), C/N/O (2s, 2p), P (3s, 3p), Br (4s, 4p), I (5s, 5p), and Pb (6s, 6p). A plane-wave basis set with a cut-off energy of 700 eV was chosen for these calculations. The $MAPbI_3$ (110) surface was modeled using a slab supercell model with a 30 Å vacuum gap along the c-axis to prevent interaction between periodic images. Bulk calculations utilized a 4 × 4 × 3 k-point mesh, while surface interactions were analyzed using a 1 × 1 × 1 k-point mesh. Structural optimization continued until the Hellmann–Feynman forces were reduced to 0.05 eV Å^{-1}. For slab relaxation, the top layer was allowed to relax, while the bottom layer was fixed to simulate the bulk-like conditions. Adsorption energies ($E_{ads.}$) were calculated using the relationship:

$$E_{\mathbf{ads.}} = E_{\mathbf{sub.-ads.}} - E_{\mathbf{sub.}} - E_{\mathbf{mol.}}$$

where $E_{sub.-ads.}$ is total energy of the substrate with the adsorbed molecule, $E_{sub.}$ is the energy of the clean substrate, and $E_{mol.}$ is the energy of the isolated adsorbate molecule. Charge density differences were calculated by subtracting the charge densities of the pristine surface and the isolated molecule from the charge density of the surface with the adsorbed molecule. Crystal structure visualizations and charge density maps were generated using the VESTA software [55].

3. Results and discussion

To optimize the PTAA/perovskite interface, we synthesized a novel molecular modifier, 3Br-Cz-4PA, which is a monobromo-carbazole linked to a phosphonic acid group via a butyl chain (Fig. 1a). Conventional carbazole-based SAMs typically exhibit a symmetrical configuration, which often results in a weak dipole and less effective π-π stacking interactions [56,57]. We strategically designed 3Br-Cz-4PA with a single bromine atom positioned asymmetrically on the carbazole core and synthesized it to form an interfacial layer on the HTL. This asymmetry was intended to balance steric hindrance and π-π stacking interactions during SAM formation. Supporting computational analyses (Fig. S3) provide that the asymmetrical structure of 3Br-Cz-4PA exhibits a distinct dipole moment vector and a localized electrostatic potential, making it a unique and highly effective interfacial modifier. We integrated 3Br-Cz-4PA by spin-coating it onto the PTAA substrate, followed by a solvent wash to remove unadsorbed overlayers, creating a modified layer termed PTAA-3Br. Fig. 1b schematically represents the planar p-i-n device structure, consisting of sequential layers: ITO/PTAA/3Br-Cz-4PA/$MAPbI_3$/$PC_{61}BM$/BCP/Ag. The modification of PTAA surfaces with 3Br-Cz-4PA was confirmed by X-ray photoelectron spectroscopy (XPS). XPS analyses showed the expected C 1s and N 1s peaks corresponding to PTAA component (Fig. S4), with the additional Br 3d peak at around 71 eV in PTAA-3Br films, indicating the presence of 3Br-Cz-4PA molecules (Fig. 1c). SEM and AFM images (Fig. S5) showed no significant morphological changes before and after 3Br-Cz-4PA deposition, likely due to the ultra-thin nature of the 3Br-Cz-4PA layer. This inference is supported by UV–Vis transmittance spectra (Fig. 1d), which indicate that the transmittance of PTAA films on ITO substrates remains above 90 % across the 450–900 nm wavelength range, irrespective of the treatment. This observation implies an absence of parasitic loss from the 3Br-Cz-4PA layer, suggesting that it likely form an ultra-thin coverage on PTAA. Furthermore, elemental distribution, ascertained through

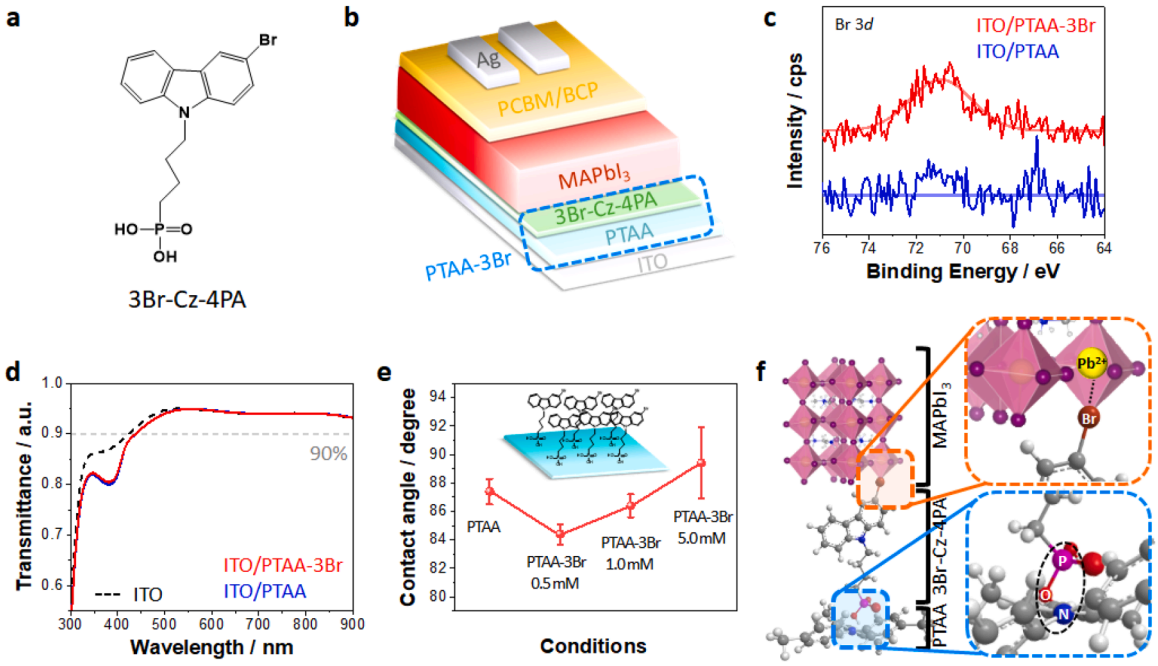

Fig. 1. (a) Molecular structure of 3Br-Cz-4PA. (b) Device structure of the inverted PSC with PTAA-3Br as the HTL interface. (c) Br 3d XPS spectra of pristine PTAA and PTAA-3Br films on ITO substrates. (d) UV–Vis transmittance spectra of ITO/PTAA and ITO/PTAA-3Br films. (e) Water contact angle measurement of ITO/PTAA and ITO/PTAA-3Br with different concentrations of 3Br-Cz-4PA. The standard deviation was obtained from three individual measurements for each sample. (f) Schematic diagram illustrating the chemical interactions between PTAA and 3Br-Cz-4PA (blue square) and between 3Br-Cz-4PA and $MAPbI_3$ (orange square).

energy dispersive X-ray spectroscopy (EDX) (Fig. S6), confirmed a uniform coverage of Br, validating the high-quality molecular layer formation. The surface chemistry and orientation of 3Br-Cz-4PA molecules on PTAA were also investigated using water contact angle (CA) measurements (Fig. 1e). An initial decrease in hydrophobicity at 0.5 mM concentration of 3Br-Cz-4PA suggests a vertical orientation facilitated by chemical bonding between PTAA and 3Br-Cz-4PA, while an increase in hydrophobicity at higher concentrations is due to the increased presence of hydrophobic Br moieties [58]. Based on this observation, Fig. 1f illustrates the proposed chemical interaction of 3Br-Cz-4PA at the buried interface. The acid-base interaction likely occurs between the –P–OH group of 3Br-Cz-4PA and the nitrogen in the PTAA backbone during the molecular layer formation. According to previous research, the –P–OH group within the $–PO_3H_2$ moiety of 3Br-Cz-4PA, possessing acidic properties, is presumed to form an acid-base interaction with the nitrogen in the PTAA backbone, which has lone pair electrons, resulting in a $P–O^-…^+H–N–$ bond [38]. Additionally, the electron-rich Br^- substituents are hypothesized to electrostatically interact with Pb^{2+} in

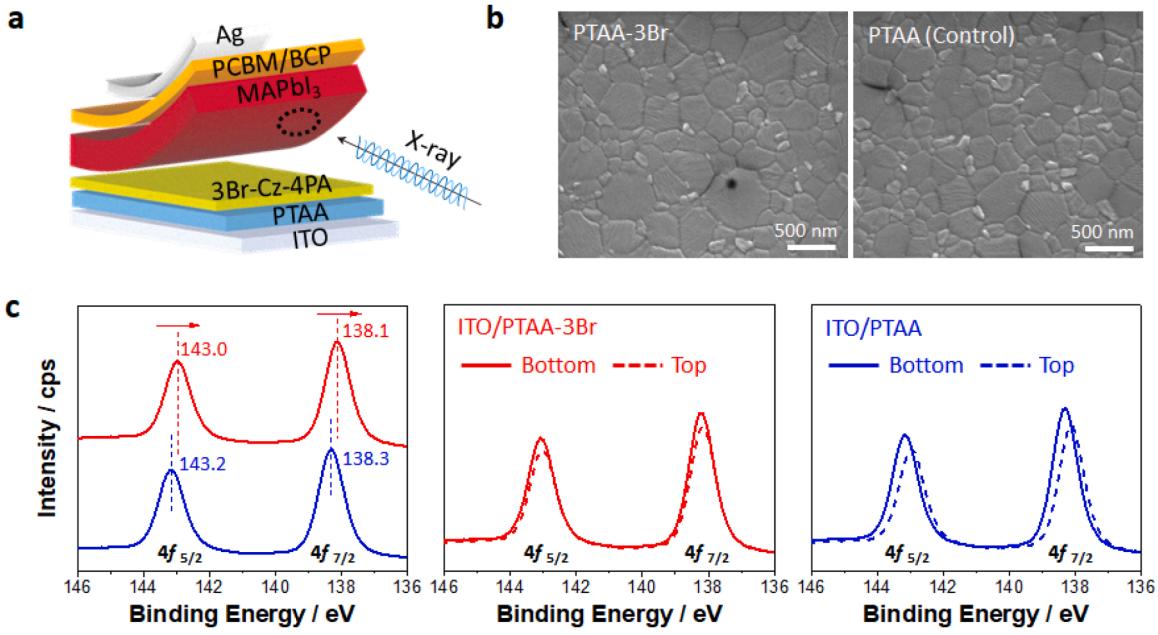

Fig. 2. (a) Schematic diagram of peeling off the buried interface of the device to investigate the bottom surface of $MAPbI_3$ film. (b) SEM images of $MAPbI_3$ bottom surface peeled off from PTAA-3Br and PTAA (control). (c) Pb 4f XPS spectra of $MAPbI_3$ films on PTAA-3Br (red) and PTAA (blue): bottom (straight line) and top (dotted line).

$MAPbI_3$, as Br can donate lone pair electrons to the empty 6p orbital of Pb^{2+} ions [59].

To verify our hypothesis, we investigated the buried surface of perovskite film peeled off from ITO/PTAA(or PTAA-3Br) substrates (Fig. 2a). To peel off the perovskite film, UV-curable epoxy resin (LOCTITE SI 5240) was applied on top of the devices, which were then covered with a cover glass. After UV exposure, the perovskite film was mechanically peeled off from the ITO/HTL substrate (Fig. S7). SEM images of the buried surface of $MAPbI_3$ exhibited well-defined grains without any degradation or HTL residue (Fig. 2b). Treatment with 3Br-Cz-4PA resulted in a smoother surface with larger perovskite crystal grains compared to the control sample. The chemical interaction between the perovskite and 3Br-Cz-4PA was validated by XPS measurement. The N 1s XPS signal associated with MA^+ in $MAPbI_3$ (402.3 eV) was well resolved (Fig. S8a) and showed a shift in the buried surface of $MAPbI_3$ grown on PTAA-3Br compared to pristine PTAA, suggesting an electronic interaction between the perovskite and the introduced molecular modifier at the buried interface. Fig. 2c compares the Pb 4f XPS spectra for $MAPbI_3$ grown on both pristine and modified HTLs. A shift to lower binding energy was observed in the Pb 4f XPS signals for $MAPbI_3$ deposited on PTAA-3Br: from 138.3 and 143.2 eV to 138.1 and 143.0 eV for Pb $4f_{7/2}$ and $4f_{5/2}$, respectively. This suggests a reduction in the cationic charge of Pb^{2+} ions, likely due to coordination bonding between Br and Pb^{2+} [60–63]. This indicates that 3Br-Cz-4PA can passivate the undercoordinated Pb^{2+} ions, which in turn suppress the formation of metallic Pb. Importantly, the similarity in the Pb 4f signals for both the top and buried (bottom) surfaces of $MAPbI_3$ on PTAA-3Br, in contrast to the variation seen with pristine PTAA, signifies the role of 3Br-Cz-4PA in minimizing undercoordinated Pb^{2+} defects during perovskite crystallization. Likewise, after modification with 3Br-Cz-4PA, as shown in Fig. S8b, the binding energy of I 3d peaks exhibited a slight downward shift from 619.3 and 630.8 eV to 619.1 and 630.6 eV. This indicates that 3Br-Cz-4PA could simultaneously passivate the cationic defects such as undercoordinated Pb^{2+} and halide vacancies at the buried interface. In summary, based on XPS results, 3Br-Cz-4PA promotes complete PbX_6 octahedral coordination and contributes to a more robust buried interface by passivating interfacial defects, especially at buried interface. This confirms that the 3Br-Cz-4PA modification can correct the stoichiometry of perovskite materials and suppress interfacial losses.

DFT calculations further substantiate our hypothesis that 3Br-Cz-4PA acts as a chemical bridge between the PTAA and $MAPbI_3$ layers, as shown in Fig. 1f. These calculations focused on the PbI_2-terminated (110) surface of $MAPbI_3$, evaluating the passivation effect of the 3Br-Cz-4PA molecule on undercoordinated surface Pb cations. Calculated adsorption energies ($E_{ads.}$) (Fig. 3a and Table S1) reveal that $MAPbI_3$ forms a stronger binding with 3Br-Cz-4PA ($E_{ads.} = -3.93$ eV) compared to PTAA ($E_{ads.} = -3.82$ eV), indicating a preference for the 3Br-Cz-PA molecule at the interface. Additionally, as depicted in Fig. 3b, the distance between the surface Pb and the nearest N atom of the PTAA molecule is approximately 4.71 Å, which is significantly larger than the typical Pb–I bond length of around 3.2 Å. In comparison, as illustrated in Fig. 3c, the bond length from the surface Pb to the nearest Br atom of the 3Br-Cz-4PA molecule is much shorter at 3.45 Å. This optimal proximity supports the formation of stable Pb-Br bonds, facilitating the completion of the octahedral coordination within the PbX_6 framework (X being I or Br) and is crucial for reducing the deep-level defect states that negatively impact PSC performance. Charge density difference analyses, shown in Fig. 3b–c, underscore a more pronounced charge transfer from $MAPbI_3$ to 3Br-Cz-4PA than to PTAA, indicating a stronger chemical interaction at the 3Br-Cz-4PA-modified interface. The two-dimensional mapping of

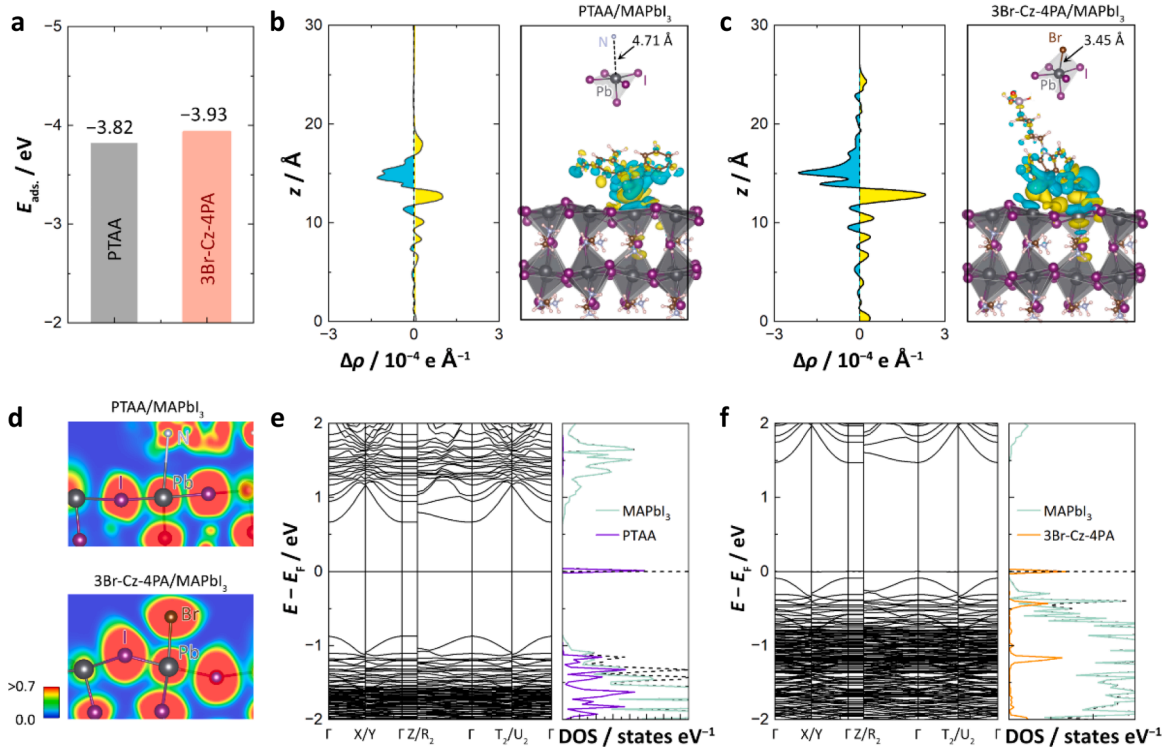

Fig. 3. Calculated adsorption energies, charge density differences, and the electronic structures of PTAA/$MAPbI_3$ and 3Br-Cz-4PA/$MAPbI_3$. (a) Comparison of the adsorption energies between PTAA/$MAPbI_3$ and 3Br-Cz-4PA/$MAPbI_3$. Detailed information on the total energies is provided in Table S1. (b–c) Charge density differences (right panel) and planar-averaged charge density differences (left panel) of (b) PTAA/$MAPbI_3$ and (c) 3Br-Cz-4PA/$MAPbI_3$. The yellow and blue surfaces represent positive and negative isosurfaces, respectively. The inset shows the local structure around the surface Pb atom serving as an adsorption site. (d) Two-dimensional plots of the electron localization function for PTAA/$MAPbI_3$ (upper panel) and 3Br-Cz-4PA/$MAPbI_3$ (lower panel). (e–f) Electronic band structures and the density of states (DOS) for the (e) PTAA/$MAPbI_3$ and (f) 3Br-Cz-4PA/$MAPbI_3$. The projected DOSs for the surface Pb atom and the nearest atom of the adsorbed molecules are provided in Fig. S9.

the electron localization function (Fig. 3d) also supports the stronger chemical interaction between the surface Pb cation and the Br anion of the 3Br-Cz-4PA. The electronic structure implications of this interaction are evident in Fig. 3e and f. The highest occupied molecular orbital (HOMO) of PTAA does not exhibit significant hybridization with the valence band of $MAPbI_3$, resulting in deep-level defect states. In contrast, the HOMO of 3Br-Cz-4PA shows pronounced hybridization with the valence band edge of $MAPbI_3$. Such chemical bonding, indicated by the formation of Pb–Br bonds, is likely a substantial factor behind the improved reproducibility of device performance in our study.

To evaluate the influence of our interface engineering on perovskite film formation, we compared the grain size and crystal structure of the films on ITO/PTAA-3Br with those on a control HTL. This comparative study employed SEM and X-ray diffraction (XRD), with a PTAA layer pre-wetted with dimethylformamide (PTAA-DMF) serving as the control due to the low reproducibility of devices with pristine PTAA (Fig. S10). The DMF treatment was previously reported to reduce pinhole presence in perovskite films [29,30]. SEM analysis reveals a stark contrast between the two HTLs (Fig. 4a). The PTAA-DMF HTLs resulted in perovskite films characterized by smaller grains, averaging 180 ± 50 nm, with numerous grain boundaries visible in cross-section. In comparison, the perovskite films deposited on PTAA-3Br HTLs exhibited significantly larger and more uniform grains, averaging 260 ± 80 nm, with a notable absence of pinholes, indicative of superior grain growth facilitated by the interface engineering strategy. These morphological improvements correlate with the XRD patterns (Fig. 4b), where the $MAPbI_3$ films on PTAA-3Br display a sharper and more pronounced (002)/(110) peak at 14.1°, suggesting enhanced crystallization over those on PTAA-DMF. We also explored the interfacial tension between the solid HTL surface and the perovskite precursor solution through CA measurements (Fig. 4c). It is theorized that reducing the wettability of the HTLs to perovskite precursor solutions may suppress heterogeneous nucleation, consequently increasing the critical free energy barrier. This change discourages the formation of dense nuclei and promotes grain boundary migration, culminating in the growth of larger perovskite grains [64, 65]. Our results confirm this hypothesis; treatment with 3Br-Cz-4PA increased the hydrophobicity of the PTAA surface, as demonstrated by the CA measurements. This hydrophobic modification promotes grain growth, as supported by the SEM images and XRD results presented. We anticipate that the improved crystallization and reduced grain boundaries will have a beneficial impact on device performance and stability, which we will explore in further sections of this discussion.

To investigate the defect passivation efficacy of 3Br-Cz-4PA at buried interface, we characterized the optoelectronic properties of the perovskite film and device stacks. First, we executed space-charge limited current (SCLC) measurement to characterize the presence of defects within the perovskite crystal structures. The SCLC curves of the hole-only devices, configured as ITO/PTAA-DMF or PTAA-3Br/$MAPbI_3$/PTAA/Ag, are showcased in Fig. 5a. From these curves, we derived the trap-filled limit voltage (V_{TFL}) and estimated the density of trap states (N_d) using the relation $N_d = 2\varepsilon\varepsilon_0 V_{TFL}/eL^2$, where ε is the relative dielectric constant of the perovskite layer, ε_0 is the vacuum permittivity, e represents the elementary charge, and L denotes the thickness of the perovskite layer. Adopting a dielectric constant of 32, as characteristic of single-crystal $MAPbI_3$ [66], we discerned a V_{TFL} of 0.616 V and an N_d of 8.72×10^{15} cm^{-3} for PTAA-DMF/perovskite, which decreased to 0.504 V and 7.14×10^{15} cm^{-3} for PTAA-3Br/perovskite configuration, evidencing a significant reduction in defect density due to the implementation of the 3Br-Cz-4PA interlayer. Furthermore, to identify the suppression of non-radiative recombination through effective reduction in trap defects, the ideality factor (n) was deduced from light intensity-dependent open-circuit voltage (V_{OC}) measurements in full device stacks (Fig. 5b). The slope in V_{OC} vs. light intensity plots, nk_BT/q – where k_B is the Boltzmann constant, T is the temperature, and q is the

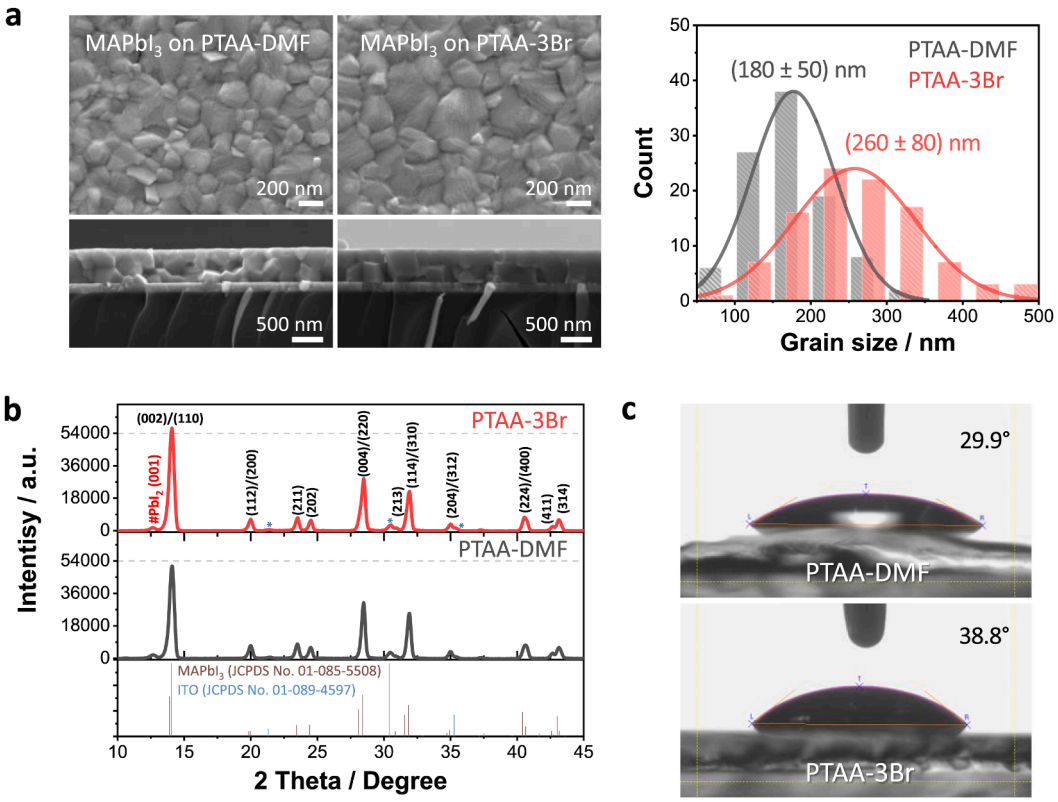

Fig. 4. (a) Top-view and cross-sectional SEM images of $MAPbI_3$ films deposited on PTAA-DMF and PTAA-3Br layers and histograms of grain size distribution. To ensure accuracy, 100 grains were counted to measure the grain size. (b) XRD patterns of perovskite films deposited on PTAA-DMF and PTAA-3Br. (c) Contact angle images of the perovskite solution on ITO/PTAA-DMF and ITO/PTAA-3Br.

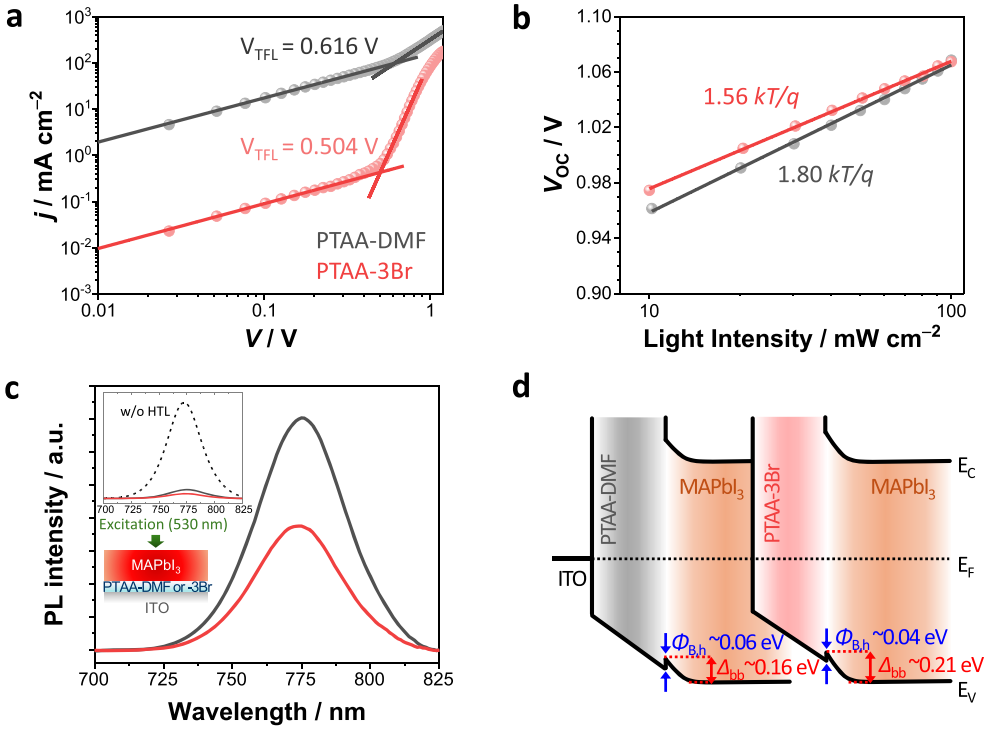

Fig. 5. (a) Dark $j-V$ curves of the hole-only devices with the structure of ITO/PTAA-DMF or PTAA-3Br/perovskite/PTAA/Ag. (b) Light-intensity-dependent V_{OC} and (c) steady-state photoluminescence spectra of PSCs fabricated on PTAA-DMF and PTAA-3Br. (d) Schematic of energy level diagrams at short circuit condition with band bending.

elementary charge – indicating a drop in n from 1.80 for the control to 1.56 for the PTAA-3Br device. A lower n suggests reduced non-radiative recombination at interfaces [38,67,68].

The steady-state photoluminescence (PL) measurement of perovskite films prepared on treated and control PTAA HTL was conducted to further probe the interface recombination and charge transfer. The PL spectra, presented in Fig. 5c, indicate a diminished PL intensity for perovskite films on PTAA-3Br in comparison to PTAA-DMF, implying a more efficient hole extraction to the PTAA-3Br layer and a concurrent decrease in interfacial recombination. Energy level alignment assessments were also executed to confirm the facilitated charge transfer in devices based on PTAA-3Br. Energy levels of ITO, PTAA-DMF, and PTAA-3Br were measured through ultraviolet photoelectron spectroscopy (UPS) measurements (Fig. S11), and the energy level of $MAPbI_3$ was referenced from literature [69]. Depicted in Fig. S12 are energy level diagrams under initial contact and short-circuit conditions. The lowest unoccupied molecular orbital (LUMO) of PTAA was estimated from its optical bandgap (E_g, 2.9 eV), derived from the UV–Vis absorption spectrum (Fig. S13). Under short-circuit conditions, even though thermodynamics would suggest a more advantageous charge transfer at the PTAA-DMF/perovskite interface owing to a closer HOMO alignment, it is the kinetic factors that are revealed by the band bending at the PTAA-3Br/perovskite junction which bolster effective charge transfer. This junction's band bending (Δ_{bb} of 0.21 eV), as shown in Fig. 5d, surpasses the PTAA-DMF/perovskite junction's (Δ_{bb} of 0.16 eV), providing a more potent electric field for hole extraction. Additionally, a reduction in the hole-injection barrier ($\Phi_{B,h}$) from 0.06 eV to 0.04 eV is noted with the 3Br-Cz-4PA modification. These UPS findings indicated that kinetic considerations, such as band bending, play a significant role in charge transfer processes, outweighing thermodynamic alignment limitations. Collectively, 3Br-Cz-4PA mediated interface engineering not only refines the contact quality between the HTL and perovskite layers but also enhances hole extraction efficiency and diminishes interface recombination. These improvements can translate into more efficient and stable perovskite solar cells.

We fabricated devices and investigated the photovoltaic performance of the PSCs with different buried interfaces using $MAPbI_3$-basd perovskite. Prior to demonstrating the effects of 3Br-Cz-4PA interface engineering on device performance, the optimal concentration of the 3Br-Cz-4PA was determined. We systematically evaluated device performance across a spectrum of concentrations and referenced statistical photovoltaic parameters detailed in Fig. S14. Despite the consistency in device performance across these concentrations, a focused examination highlighted in Fig. S15 suggested a nuanced relationship between the 3Br-Cz-4PA concentration and the morphological quality of perovskite films. At a concentration of 0.5 mM, limited perovskite grain growth was observed, likely due to the surface's relative wettability to the precursor solution (Fig. S15a). Conversely, at a higher concentration of 5 mM, we noted a significant deterioration in grain quality, particularly at the interface (as highlighted by a yellow circle in Fig. S15c). This observation suggests that elevated concentrations of 3Br-Cz-4PA may adversely affect grain structure. Consequently, we identified an optimal concentration of 1.0 mM, balancing substantial grain development while preventing the adverse effects associated with higher concentrations. This optimized concentration was thus selected for all subsequent device fabrications to ensure a controlled exploration of interface engineering impacts on PSC performance.

In pursuing advanced p-i-n PSC performance, we fabricated devices using both PTAA-DMF and PTAA-3Br HTLs and subsequently evaluated their photovoltaic responses. As shown in Fig. 6a, representative devices incorporating the 3Br-Cz-4PA SAM displayed superior performance compared to the PTAA-DMF control, achieving an enhanced average PCE of 17.9 %, relative to 16.4 % for the latter, which was mainly ascribed to the increase of short-circuit current density (j_{SC}) from 20.3 to 21.2 mA cm^{-2} and fill-factor (FF) from 77.2 to 80.5 %. The external quantum efficiency (EQE) spectra and the corresponding integrated current density values, represented in Fig. 6b, validate the j_{SC} values derived from the j–V curves (Fig. 6a). The improved j_{SC} in devices

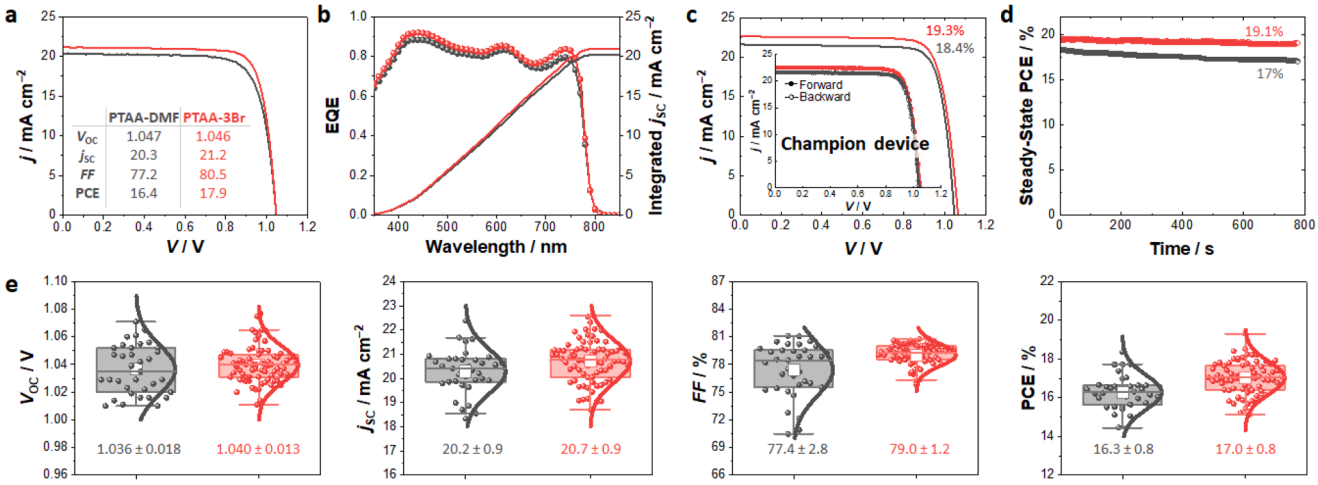

Fig. 6. (a–b) Representative device performance: (a) $j-V$ curves of representative devices with PTAA-DMF and PTAA-3Br layers and (b) corresponding EQE spectra. (c–d) Champion device performance: (c) $j-V$ curve (inset: $j-V$ curves of reversed and forward scans) and (d) steady-state PCE as a function of time measured at the fixed maximum-power-point (MPP) voltage (V_{max} = 0.897 V). (e) Statistical box charts for the photovoltaic parameters of V_{OC}, j_{SC}, *FF*, and PCE of 37 and 75 devices with PTAA-DMF and PTAA-3Br layers, respectively.

treated with 3Br-Cz-4PA is attributable to the improved film crystallinity and increased grain size, as supported by our SEM and XRD results (Fig. 4). Moreover, the incorporation of Br in the 3Br-Cz-4PA compound is thought to contribute to passivation of undercoordinated Pb^{2+} defects at the HTL/perovskite interface, as inferred from our XPS findings and DFT calculation. Fig. 6c show photovoltaic performance of best devices with PTAA-DMF and PTAA-3Br. Notably, the best-performing device with PTAA-3Br HTL exhibited a PCE of 19.3 %, with a V_{OC} of 1.07 V, a j_{SC} of 22.6 mA cm^{-2}, and a *FF* of 80.2 %. This device also showed minimal hysteresis, confirmed by the close matching of the forward and backward scans in the $j-V$ characterization depicted in inset of Fig. 6c. The steady-state PCE measurements at the maximum-power-point (MPP) voltage for these devices are presented in Fig. 6d. To demonstrate the impact of the 3Br-Cz-4PA interfacial layer, $MAPbI_3$-based perovskite was selected as a representative system. The obtained efficiency of 19.3 % aligns well with similar $MAPbI_3$-based devices as shown in Table S2.

In our systematic effort to ascertain the reproducibility of our inverted PSCs, we fabricated and characterized in excess of 30 devices across multiple production batches. The photovoltaic parameters were thoroughly recorded to assess the consistency of device performance. Fig. 6e presents the statistical distribution of these parameters, clearly demonstrating the enhanced performance and reliability of devices with the PTAA-3Br HTL. A particularly noteworthy aspect of the data is the

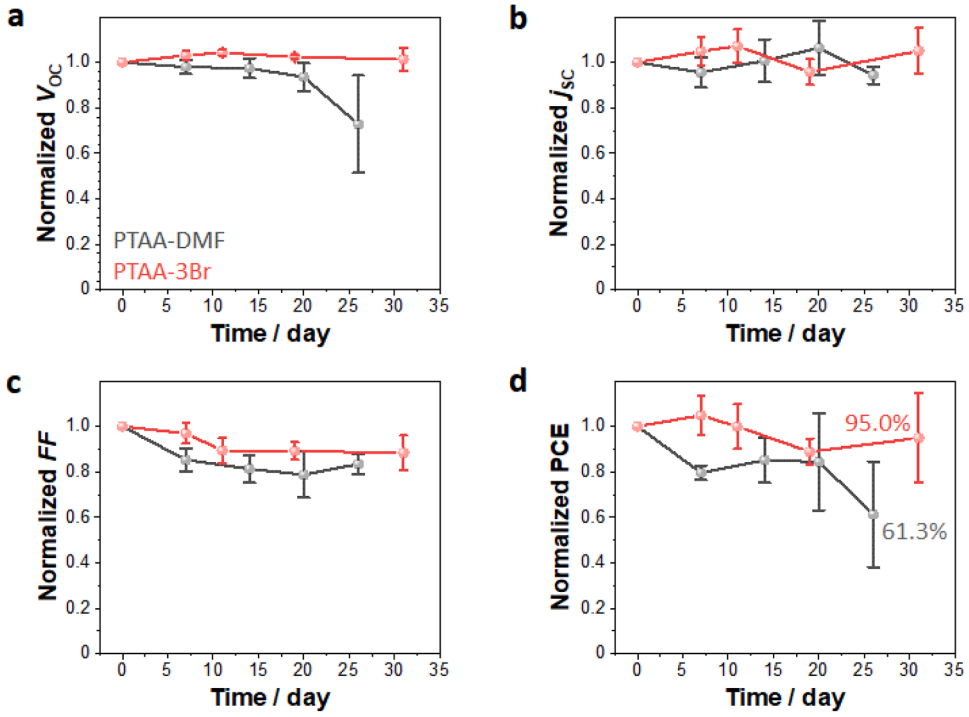

Fig. 7. Evolution of device parameters for PSCs with PTAA-DMF and PTAA-3Br as HTLs, measured in ambient air without encapsulation over 1 month: normalized (a) V_{OC}, (b) j_{SC}, (c) *FF*, and (d) PCE). The data points represent the average values from four independently fabricated devices, with error bars indicating standard deviations.

more concentrated distribution of the *FF* for the PTAA-3Br devices, suggesting greater uniformity and dependability in performance relative to their PTAA-DMF counterparts. An increment in the *FF* for PTAA-3Br devices is also discernible, achieving an average *FF* of (79.0 ± 1.2)%, which is an improvement over the (77.4 ± 2.8)% observed for PTAA-DMF devices. This elevation in *FF* highlights not just the successful application of the 3Br-Cz-4PA interfacial modification but also suggests a refined electronic synergy within the cell architecture. Furthermore, the histograms depicting the V_{OC} and j_{SC} corroborate these observations, with PTAA-3Br devices displaying more defined distributions and pointing to enhanced uniformity in device fabrication. The observed consistency and enhanced performance in devices incorporating PTAA-3Br affirm the role of the 3Br-Cz-4PA SAM in precisely modulating interfacial characteristics, thereby contributing to the progression of PSC technology.

Moving beyond immediate performance metrics, we also investigated the stability of PSCs under ambient air storage without encapsulation (Fig. 7). The cell with PTAA-DMF HTL retained merely 61.3 % of its initial PCE after one month, whereas the PTAA-3Br HTL device preserved 95.0 % of its initial efficiency over the same period. A closer inspection of the normalized V_{OC}, j_{SC}, and *FF* over time reveals the critical role that V_{OC} stability play in the enhanced durability of the PSCs. Given that the degradation of interfacial layers and trap-assisted recombination notably affect V_{OC} within PSCs [70], the marked improvement in device stability with the PTAA-3Br can be largely ascribed to the robust interface between the HTL and perovskite layer, improved film crystallinity, and a reduced defect density. Furthermore, as shown in Fig. S16, photographs of the completed devices taken nearly 3 months after their fabrication clearly demonstrate the superior stability of the PTAA-3Br HTL device. In contrast, the PTAA-DMF device exhibits a pronounced color change in the perovskite film, transitioning from dark brown to yellow, indicative of severe material degradation. This observation is further supported by the cross-sectional SEM images (Fig. S17), which reveal substantial structural damage and void formation at the buried interface of the PTAA-DMF device. Conversely, the PTAA-3Br device maintains a more intact and uniform interface, underscoring the robustness of the PTAA-3Br HTL in preserving device integrity over extended periods.

4. Conclusions

In summary, our study has introduced a sophisticated approach to molecular interface engineering through the deployment of a monobromo-carbazole-based SAM, 3Br-Cz-4PA, which significantly reinforces the interface between PTAA HTLs and $MAPbI_3$ perovskites. The judicious integration of 3Br-Cz-4PA acts as an effective intermediary at the PTAA/perovskite junction, leading to noteworthy improvements in the performance, reproducibility, and durability of perovskite solar cells. This interfacial modification has pronouncedly enhanced the quality of perovskite films, evident in the increased grain size, augmented crystallinity, and successful passivation of interfacial Pb^{2+} defects. It has also propelled an improvement in hole extraction efficiency and reduced non-radiative recombination, contributing to a remarkable PCE of 19.3 %. Notably, the solar cells with the PTAA-3Br interface have maintained 95 % of their initial efficiency after prolonged exposure to ambient air, circumventing the need for encapsulation. These breakthroughs highlight the transformative impact of interface engineering on advancing PSC technology and lay the groundwork for subsequent innovations in this rapidly evolving domain.

CRediT authorship contribution statement

Uijoon Lee: Writing – original draft, Methodology, Investigation, Formal analysis, Data curation. **Min Kyoung Shin:** Writing – original draft, Methodology, Investigation, Formal analysis, Data curation. **Heejun Lee:** Writing – original draft, Visualization, Software, Investigation, Formal analysis. **Byungsoo Kang:** Validation, Investigation, Data curation. **Minseok Kim:** Validation, Investigation, Data curation. **Sooyoung Han:** Validation, Investigation, Data curation. **Taehee Kim:** Investigation, Formal analysis, Data curation. **Hae Jung Son:** Investigation, Formal analysis, Data curation. **Phillip Lee:** Writing – review & editing, Validation, Supervision. **Rongrong Cheacharoen:** Writing – review & editing, Methodology, Investigation, Formal analysis. **Dong Hoe Kim:** Writing – review & editing, Validation, Supervision. **Joonho Bang:** Writing – review & editing, Validation, Supervision, Project administration, Methodology, Funding acquisition. **Jongin Hong:** Writing – review & editing, Validation, Supervision, Project administration, Methodology, Funding acquisition, Conceptualization. **Yoon Hee Jang:** Conceptualization, Supervision, Project administration, Data curation, Validation, Funding acquisition, Writing – review & editing.

Declaration of competing interest

The authors declare that they have no known competing financial interests or personal relationships that could have appeared to influence the work reported in this paper.

Acknowledgements

This work was supported by the KIST Institutional Program; the Basic Science Research Program through the National Research Foundation (NRF) of Korea funded by the Ministry of Science and ICT [NRF-2021R1A2C2011893]; the NRF funded by the Ministry of Education [Regional Innovation Strategy (RIS) 2021RIS-003]; Korea Institute of Energy Technology Evaluation and Planning (KETEP) grant funded by the Ministry of Trade, Industry & Energy (MOTIE) [RS-2021-KP002504, Convergence Graduate School of Intelligent Energy and Industry]. The authors would like to thank Dini Hayati from the National Research and Innovation Agency (BRIN), Indonesia, for performing the dipole moment vector and ESP map calculations. The authors also thank Daeun Lee and Hyunju Kim for their technical support in device fabrication and Won Kook Choi from KIST for technical assistance in PL measurements.

Supplementary materials

Supplementary material associated with this article can be found, in the online version, at doi:10.1016/j.surfin.2025.106094.

Data availability

The data that support the findings of this study are available from the corresponding author upon reasonable request.

References

[1] NREL, Best Research-Cell Efficiency Chart (2024). https://www.nrel.gov/pv/cell-efficiency.html. assessed 22 July.
[2] S. Bai, P. Da, C. Li, Z. Wang, Z. Yuan, F. Fu, M. Kawecki, X. Liu, N. Sakai, J.T.-W. Wang, S. Huettner, S. Buecheler, M. Fahlman, F. Gao, H.J. Snaith, Planar perovskite solar cells with long-term stability using ionic liquid additives, Nature 571 (2019) 245–250, https://doi.org/10.1038/s41586-019-1357-2.
[3] N.-G. Park, K. Zhu, Scalable fabrication and coating methods for perovskite solar cells and solar module, Nat. Rev. Mater. 5 (2020) 333–350, https://doi.org/10.1038/s41578-019-0176-2.
[4] Y. Deng, S. Xu, S. Chen, X. Xiao, J. Zhao, J. Huang, Defect compensation in formamidinium–caesium perovskites for highly efficient solar mini-modules with improved photostability, Nat. Energy 6 (2021) 633–641, https://doi.org/10.1038/s41560-021-00831-8.
[5] E. Aydin, E. Ugur, B.K. Yildirim, T.G. Allen, P. Dally, A. Razzaq, F. Cao, L. Xu, B. Vishal, A. Yazmaciyan, A.A. Said, S. Zhumagali, R. Azmi, M. Babics, A. Fell, C. Xiao, S. De Wolf, Enhanced optoelectronic coupling for perovskite-silicon tandem solar cells, Nature 623 (2023) 732–738, https://doi.org/10.1038/s41586-023-06667-4.
[6] M. Jošt, E. Köhnen, A. Al-Ashouri, T. Bertram, Š. Tomšič, A. Magomedov, E. Kasparavicius, T. Kodalle, B. Lipovšek, V. Getautis, R. Schlatmann, C. A. Kaufmann, S. Albrecht, M. Topič, Perovskite/CIGS tandem solar cells: from

certified 24.2% toward 30% and beyond, ACS Energy Lett. 7 (2022) 1298–1307, https://doi.org/10.1021/acsenergylett.2c00274.
[7] R. Lin, Y. Wang, Q. Lu, B. Tang, J. Li, H. Gao, Y. Gao, H. Li, C. Ding, J. Wen, P. Wu, C. Liu, S. Zhao, K. Xiao, Z. Liu, C. Ma, Y. Deng, L. Li, F. Fan, H. Tan, All-perovskite tandem solar cells with 3D/3D bilayer perovskite heterojunction, Nature 620 (2023) 994–1000, https://doi.org/10.1038/s41586-023-06278-z.
[8] Q. Jiang, J. Tong, Y. Xian, R.A. Kerner, S.P. Dunfield, C. Xiao, R.A. Scheidt, D. Kuciauskas, X. Wang, M.P. Hautzinger, R. Tirawat, M.C. Beard, D.P. Fenning, J. J. Berry, B.W. Larson, Y. Yan, K. Zhu, Surface reaction for efficient and stable inverted perovskite solar cells, Nature 611 (2022) 278–283, https://doi.org/10.1038/s41586-022-05268-x.
[9] Z. Li, B. Li, X. Wu, S.A. Sheppard, S. Zhang, D. Gao, N.J. Long, Z. Zhu, Organometallic-functionalized interfaces for highly efficient inverted perovskite solar cells, Science 376 (2022) 416–420, https://doi.org/10.1126/science.abm8566.
[10] Z.Liang H.Xu, J. Ye, Y. Zhang, Z. Wang, H. Zhang, C. Wan, G. Xu, J. Zeng, B. Xu, Z. Xiao, T. Kirchartz, X. Pan, Constructing robust heterointerface for carrier viaduct via interfacial molecular bridge enables efficient and stable inverted perovskite solar cell, Energy Environ. Sci. 16 (2023) 5792–5804, https://doi.org/10.1039/D3EE02591H.
[11] H. Chen, C. Liu, J. Xu, A. Maxwell, W. Zhou, Y. Yang, Q. Zhou, A.S.R. Bati, H. Wan, Z. Wang, L. Zheg, J. Wang, P. Serles, Y. Liu, S. Teale, Y. Liu, M.I. Saidaminov, M. Li, N. Rolston, S. Hoogland, T. Filleter, M.G. Kanatzidis, B. Chen, Z. Ning, E. H. Sargent, Improved charge extraction in inverted perovskite solar cells with dual-site-binding ligands, Science 384 (2024) 189–193, https://doi.org/10.1126/science.adm9474.
[12] S. Liu, J. Li, W. Xiao, R. Chen, Z. Sun, Y. Zhang, X. Lei, S. Hu, M. Kober-Czerny, J. Wang, F. Ren, Q. Zhou, H. Raza, Y. Gao, Y. Ji, S. Li, H. Li, L. Qiu, W. Huang, Y. Zhao, B. Xu, Z. Liu, H.J. Snaith, N.-G. Park, W. Chen, Buried interface molecular hybrid for inverted perovskite solar cells, Nature 632 (2024) 536–542, https://doi.org/10.1038/s41586-024-07723-3.
[13] D. Li, Y. Huang, Z. Ren, A. Amini, A.B. Djurišić, C. Cheng, G. Li, Recent progress of inverted organic-inorganic halide perovskite solar cells, J. Energy Chem. 79 (2023) 168–191, https://doi.org/10.1016/j.jechem.2022.12.029.
[14] S. Liu, V.P. Biju, Y. Qi, W. Chen, Z. Liu, Recent progress in the development of high-efficiency inverted perovskite solar cells, NPG Asia Mater. 15 (2023) 27, https://doi.org/10.1038/s41427-023-00474-z.
[15] R. Li, X. Liu, J. Chen, Opportunities and challenges of hole transport materials for high-performance inverted hybrid-perovskite solar cells, Exploration 3 (2023) 20220027, https://doi.org/10.1002/EXP.20220027.
[16] L. Li, M. Wei, V. Carnevali, H. Zeng, M. Zeng, R. Liu, N. Lempesis, F.T. Eickemeyer, L. Luo, L. Agosta, M. Dankl, S.M. Zakeeruddin, U. Roethlisberger, M. Grätzel, Y. Rong, X. Li, Buried interface engineering enables efficient and 1960-hour ISOS-L-2I stable inverted perovskite solar cells, Adv. Mater. 36 (2023) 2303869, https://doi.org/10.1002/adma.202303869.
[17] S. Ye, H. Rao, M. Feng, L. Xi, Z. Yen, D.H.L. Seng, Q. Xu, C. Boothroyd, B. Chen, Y. Guo, B. Wang, T. Salim, Q. Zhang, H. He, Y. Wang, X. Xiao, Y.M. Lam, T.C. Sum, Expanding the low-dimensional interface engineering toolbox for efficient perovskite solar cells, Nat. Energy 8 (2023) 284–293, https://doi.org/10.1038/s41560-023-01204-z.
[18] J.H. Heo, H.J. Han, D. Kim, T.K. Ahn, S.H. Im, Hysteresis-less inverted $CH_3NH_3PbI_3$ planar perovskite hybrid solar cells with 18.1 % power conversion efficiency, Energy Environ. Sci. 8 (2015) 1602–1608, https://doi.org/10.1039/C5EE00120J.
[19] A. Al-Ashouri, A. Magomedov, M. Roß, M. Jošt, M. Talaikis, G. Chistiakova, T. Bertram, J.A. Márquez, E. Köhnen, E. Kasparavičius, S. Levcenco, L. Gil-Escrig, C.J. Hages, R. Schlatmann, B. Rech, T. Malinauskas, T. Unold, C.A. Kaufmann, L. Korte, G. Niaura, V. Getautis, S. Albrecht, Conformal monolayer contacts with lossless interfaces for perovskite single junction and monolithic tandem solar cells, Energy Environ. Sci. 12 (2019) 3356–3369, https://doi.org/10.1039/C9EE02268F.
[20] S. Sajid, S. Alzahmi, I.B. Salem, J. Park, I.M. Obaidat, Inorganic hole transport materials in perovskite solar cells are catching up, Mater. Today Energy 37 (2023) 101378, https://doi.org/10.1016/j.mtener.2023.101378.
[21] F.M. Rombach, S.A. Haque, T.J. Macdonald, Lessons learned from spiro-OMeTAD and PTAA in perovskite solar cells, Energy Environ. Sci. 14 (2021) 5161–5190, https://doi.org/10.1039/D1EE02095A.
[22] M. Stolterfoht, C.M. Wolff, Y. Amir, A. Paulke, L. Perdigón-Toro, P. Caprioglio, D. Neher, Approaching the fill factor Shockley–Queisser limit in stable, dopant-free triple cation perovskite solar cells, Energy Environ. Sci. 10 (2017) 1530–1539, https://doi.org/10.1039/C7EE00899F.
[23] Y. Wang, L. Duan, M. Zhang, Z. Hameiri, X. Liu, Y. Bai, X. Hao, PTAA as efficient hole transport materials in perovskite solar cells: a review, Sol. RRL. 6 (2022) 2200234, https://doi.org/10.1002/solr.202200234.
[24] W. Zhang, J. Smith, R. Hamilton, M. Heeney, J. Kirkpatrick, K. Song, S.E. Watkins, T. Anthopoulos, I. McCulloch, Systematic improvement in charge carrier mobility of air stable triarylamine copolymers, J. Am. Chem. Soc. 131 (2009) 10814–10815, https://doi.org/10.1021/ja9034818.
[25] F. Hou, B. Shi, T. Li, C. Xin, Y. Ding, C. Wei, G. Wang, Y. Li, Y. Zhao, X. Zhang, Efficient and stable perovskite solar cell achieved with bifunctional interfacial layers, ACS Appl. Mater. Interfaces 11 (2019) 25218–25226, https://doi.org/10.1021/acsami.9b06424.
[26] F.H. Isikgor, A.S. Subbiah, M.K. Eswaran, C.T. Howells, A. Babayigit, M. De Bastiani, E. Yengel, J. Liu, F. Furlan, G.T. Harrison, S. Zhumagali, J.I. Khan, F. Laquai, T.D. Anthopoulos, I. McCulloch, U. Schwingenschlögl, S. De Wolf, Scaling-up perovskite solar cells on hydrophobic surfaces, Nano Energy 81 (2021) 105633, https://doi.org/10.1016/j.nanoen.2020.105633.
[27] K.O. Brinkmann, J. He, F. Schubert, J. Malerczyk, C. Kreusel, F. van gen Hassend, S. Weber, J. Song, J. Qu, T. Riedl, Extremely robust gas-quenching deposition of halide perovskites on top of hydrophobic hole transport materials for inverted (p–i–n) solar cells by targeting the precursor wetting issue, ACS Appl. Mater. Interfaces 11 (2019) 40172–40179, https://doi.org/10.1021/acsami.9b15867.
[28] S. Zhang, M. Stolterfoht, A. Armin, Q. Lin, F. Zu, J. Sobus, H. Jin, N. Koch, P. Meredith, P.L. Burn, D. Neher, Interface engineering of solution-processed hybrid organohalide perovskite solar cells, ACS Appl. Mater. Interfaces 10 (2018) 21681–21687, https://doi.org/10.1021/acsami.8b02503.
[29] Y. Li, C. Liang, G. Wang, J. Li, S. Chen, S. Yang, G. Xing, H. Pan, Two-step solvent post-treatment on PTAA for highly efficient and stable inverted perovskite solar cells, Photon. Res. 8 (2020) A39–A49, https://doi.org/10.1364/PRJ.398529.
[30] M. Degani, Q. An, M. Albaladejo-Siguan, Y.J. Hofstetter, C. Cho, F. Paulus, G. Grancini, Y. Vaynzof, 23.7% Efficient inverted perovskite solar cells by dual interfacial modification, Sci. Adv. 7 (2021), https://doi.org/10.1126/sciadv.abj7930 eabj7930.
[31] S. Tian, J. Chen, X. Lian, Y. Wang, Y. Zhang, W. Yang, G. Wu, W. Qiu, H. Chen, Engineering the underlying surface to manipulate the growth of 2D perovskites for highly efficient solar cells, J. Mater. Chem. A 7 (2019) 14027–14032, https://doi.org/10.1039/C9TA03022K.
[32] Q. Zhou, J. Qiu, Y. Wang, M. Yu, J. Liu, X. Zhang, Multifunctional chemical bridge and defect passivation for highly efficient inverted perovskite solar cells, ACS Energy Lett. 6 (2021) 1596–1606, https://doi.org/10.1021/acsenergylett.1c00291.
[33] E.D. Jung, A.K. Harit, D.H. Kim, C.H. Jang, J.H. Park, S. Cho, M.H. Song, H.Y. Woo, Multiply charged conjugated polyelectrolytes as a multifunctional interlayer for efficient and scalable perovskite solar cells, Adv. Mater. 32 (2020) 2002333, https://doi.org/10.1002/adma.202002333.
[34] M. Stolterfoht, C.M. Wolff, J.A. Márquez, S. Zhang, C.J. Hages, D. Rothhardt, S. Albrecht, P.L. Burn, P. Meredith, T. Unold, D. Neher, Visualization and suppression of interfacial recombination for high-efficiency large-area pin perovskite solar cells, Nat. Energy 3 (2018) 847–854, https://doi.org/10.1038/s41560-018-0219-8.
[35] Z. Gu, L. Zuo, T.T. Larsen-Olsen, T. Ye, G. Wu, F.C. Krebs, H. Chen, Interfacial engineering of self-assembled monolayer modified semi-roll-to-roll planar heterojunction perovskite solar cells on flexible substrates, J. Mater. Chem. A 3 (2015) 24254–24260, https://doi.org/10.1039/C5TA07008B.
[36] Q. Wang, C.-C. Chueh, T. Zhao, J. Cheng, M. Eslamian, W.C.H. Choy, A.K.-Y. Jen, Effects of self-assembled monolayer modification of nickel oxide nanoparticles layer on the performance and application of inverted perovskite solar cells, ChemSusChem 10 (2017) 3794–3803, https://doi.org/10.1002/cssc.201701262.
[37] N. Phung, M. Verheijen, A. Todinova, K. Datta, M. Verhage, A. Al-Ashouri, H. Köbler, X. Li, A. Abate, S. Albrecht, M. Creatore, Enhanced self-assembled monolayer surface coverage by ALD NiO in p-i-n perovskite solar cells, ACS Appl. Mater. Interfaces 14 (2022) 2166–2176, https://doi.org/10.1021/acsami.1c15860.
[38] H. Bi, Y. Fujiwara, G. Kapil, D. Tavgeniene, Z. Zhang, L. Wang, C. Ding, S. R. Sahamir, A.K. Baranwal, Y. Sanehira, K. Takeshi, G. Shi, T. Bessho, H. Segawa, S. Grigalevicius, Q. Shen, S. Hayase, Perovskite solar cells consisting of PTAA modified with monomolecular layer and application to all-perovskite tandem solar cells with efficiency over 25 %, Adv. Funct. Mater. 33 (2023) 2300089 https://doi.org/10.1002/adfm.202300089.
[39] Y. Tan, X. Chang, J.-X. Zhong, W. Feng, M. Yang, T. Tian, L. Gong, W.-Q. Wu, Chemical linkage and passivation at buried interface for thermally stable inverted perovskite solar cells with efficiency over 22 %, CCS Chem. 5 (2023) 1802–1814, https://doi.org/10.31635/ccschem.022.202202154.
[40] A. Ulman, Formation and structure of self-assembled monolayers, Chem. Rev. 96 (1996) 1533–1554, https://doi.org/10.1021/cr9502357.
[41] F. Ali, C. Roldán-Carmona, M. Sohail, M.K. Nazeeruddin, Applications of self-assembled monolayers for perovskite solar cells interface engineering to address efficiency and stability, Adv. Energy Mater. 10 (2020) 2002989, https://doi.org/10.1002/aenm.202002989.
[42] W. Jiang, F. Li, M. Li, F. Qi, F.R. Lin, A.K.-Y. Jen, π-expanded carbazoles as hole-selective self-assembled monolayers for high-performance perovskite solar cells, Angew. Chem. Int. Ed. 61 (2022) e202213560, https://doi.org/10.1002/anie.202213560.
[43] I. Levine, A. Al-Ashouri, A. Musiienko, H. Hempel, A. Magomedov, A. Drevilkauskaite, V. Getautis, D. Menzel, K. Hinrichs, T. Unold, S. Albrecht, T. Dittrich, Charge transfer rates and electron trapping at buried interfaces of perovskite solar cells, Joule 5 (2021) 2915–2933, https://doi.org/10.1016/j.joule.2021.07.016.
[44] A. Ullah, K.H. Park, H.D. Nguyen, Y. Siddique, S.F.A. Shah, H. Tran, S. Park, S. In Lee, K.-K. Lee, C.-H. Han, K. Kim, S. Ahn, I. Jeong, Y.S. Park, S. Hong, Novel phenothiazine-based self-assembled monolayer as a hole selective contact for highly efficient and stable p-i-n perovskite solar cells, Adv. Energy Mater. 12 (2022) 2103175, https://doi.org/10.1002/aenm.202103175.
[45] Y. Lin, Y. Zhang, J. Zhang, M. Marcinskas, T. Malinauskas, A. Magomedov, M. Insan Nugraha, D. Kaltsas, D.R. Naphade, G.T. Harrison, A. El-Labban, S. Barlow, S. De Wolf, E. Wang, I. McCulloch, L. Tsetseris, V. Getautis, S.R. Marder, T.D. Anthopoulos, 18.9 % efficient organic solar cells based on n-doped bulk-heterojunction and halogen-substituted self-assembled monolayers as hole extracting interlayers, Adv. Energy Mater. 12 (2022) 2202503, https://doi.org/10.1002/aenm.202202503.
[46] Z. Dai, S.K. Yadavalli, M. Chen, A. Abbaspourtamijani, Y. Qi, N.P. Padture, Interfacial toughening with self-assembled monolayers enhances perovskite solar

cell reliability, Science 372 (2021) 618–622, https://doi.org/10.1126/science.abf5602.
[47] M. Pitaro, J.S. Alonso, L. Di Mario, D.G. Romero, K. Tran, T. Zaharia, M. B. Johansson, E.M.J. Johansson, M.A. Loi, A carbazole-based self-assembled monolayer as the hole transport layer for efficient and stable $Cs_{0.25}FA_{0.75}Sn_{0.5}Pb_{0.5}I_3$ solar cells, J. Mater. Chem. A 11 (2023) 11755–11766, https://doi.org/10.1039/D3TA01276J.
[48] H.-L. Yip, S.K. Hau, N.S. Baek, H. Ma, A.K.-Y. Jen, Polymer solar cells that use self-assembled-monolayer-modified ZnO/metals as cathodes, Adv. Mater. 20 (2008) 2376–2382, https://doi.org/10.1002/adma.200703050.
[49] A. Al-Ashouri, E. Köhnen, B. Li, A. Magomedov, H. Hempel, P. Caprioglio, J. A. Márquez, A.B.M. Vilches, E. Kasparavicius, J.A. Smith, N. Phung, D. Menzel, M. Grischek, L. Kegelmann, D. Skroblin, C. Gollwitzer, T. Malinauskas, M. Jošt, G. Matič, B. Rech, R. Schlatmann, M. Topič, L. Korte, A. Abate, B. Stannowski, D. Neher, M. Stolterfoht, T. Unold, V. Getautis, S. Albrecht, Monolithic perovskite/silicon tandem solar cell with>29 % efficiency by enhanced hole extraction, Science 370 (2020) 1300–1309, https://doi.org/10.1126/science.abd4016.
[50] Gaussian 09, Revision A.02, M.J. Frisch, G.W. Trucks, H.B. Schlegel, G.E. Scuseria, M.A. Robb, J.R. Cheeseman, G. Scalmani, V. Barone, G.A. Petersson, H. Nakatsuji, X. Li, M. Caricato, A. Marenich, J. Bloino, B.G. Janesko, R. Gomperts, B. Mennucci, H.P. Hratchian, J.V. Ortiz, A.F. Izmaylov, J.L. Sonnenberg, D. Williams-Young, F. Ding, F. Lipparini, F. Egidi, J. Goings, B. Peng, A. Petrone, T. Henderson, D. Ranasinghe, V.G. Zakrzewski, J. Gao, N. Rega, G. Zheng, W. Liang, M. Hada, M. Ehara, K. Toyota, R. Fukuda, J. Hasegawa, M. Ishida, T. Nakajima, Y. Honda, O. Kitao, H. Nakai, T. Vreven, K. Throssell, J.A. Montgomery, Jr., J.E. Peralta, F. Ogliaro, M. Bearpark, J.J. Heyd, E. Brothers, K.N. Kudin, V.N. Staroverov, T. Keith, R. Kobayashi, J. Normand, K. Raghavachari, A. Rendell, J.C. Burant, S.S. Iyengar, J. Tomasi, M. Cossi, J.M. Millam, M. Klene, C. Adamo, R. Cammi, J.W. Ochterski, R.L. Martin, K. Morokuma, O. Farkas, J.B. Foresman, and D.J. Fox, Gaussian, Inc., Wallingford CT, 2016.
[51] J.C. Kromann, C. Steinmann, J.H. Jensen, Improving solvation energy predictions using the SMD solvation method and semiempirical electronic structure methods, J. Chem. Phys. 149 (2018) 104102, https://doi.org/10.1063/1.5047273.
[52] P.E. Blöchl, Projector augmented-wave method, Phys. Rev. B Condens. Matter. 50 (1994) 17953–17979, https://doi.org/10.1103/PhysRevB.50.17953.
[53] J.P. Perdew, K. Burke, M. Ernzerhof, Generalized gradient approximation fade simple, Phys. Rev. Lett. 77 (1996) 3865–3868, https://doi.org/10.1103/PhysRevLett.77.3865.
[54] G. Kresse, J. Furthmüller, Efficient iterative schemes for ab initio total-energy calculations using a plane-wave basis set, Phys. Rev. B Condens. Matter. 54 (1996) 11169–11186, https://doi.org/10.1103/PhysRevB.54.11169.
[55] K. Momma, F. Izumi, VESTA 3 for three-dimensional visualization of crystal, volumetric and morphology data, J. Appl. Cryst. 44 (2011) 1272–1276, https://doi.org/10.1107/S0021889811038970.
[56] W. Jiang, F. Li, M. Li, F. Qi, F.R. Lin, A.K.-Y. Jen, π-expanded carbazoles as hole-selective self-assembled monolayers for high-performance perovskite solar cells, Angew. Chem. Int. Ed. 61 (2022) e202213560, https://doi.org/10.1002/anie.202213560.
[57] W. Wang, X. Liu, J. Wang, C. Chen, J. Yu, D. Zhao, W. Tang, Versatile self-assembled molecule enables high-efficiency wide-bandgap perovskite solar cells and organic solar cells, Adv. Energy Mater. 13 (2023) 2300694, https://doi.org/10.1002/aenm.202300694.
[58] A. Priimagi, G. Cavallo, P. Metrangolo, G. Resnati, The halogen bond in the design of functional supramolecular materials: recent advances, Acc. Chem. Res. 46 (2013) 2686–2695, https://doi.org/10.1021/ar400103r.
[59] N.K. Noel, A. Abate, S.D. Stranks, E.S. Parrott, V.M. Burlakov, A. Goriely, H. J. Snaith, Enhanced photoluminescence and solar cell performance via lewis base passivation of organic–inorganic lead halide perovskites, ACS Nano 8 (2014) 9815–9821, https://doi.org/10.1021/nn5036476.
[60] Z. Wu, M. Jiang, Z. Liu, A. Jamshaid, L.K. Ono, Y. Qi, Highly efficient perovskite solar cells enabled by multiple ligand passivation, Adv. Energy Mater. 10 (2020) 1903696, https://doi.org/10.1002/aenm.201903696.
[61] W. Zhou, D. Li, Z. Xiao, Z. Wen, M. Zhang, W. Hu, X. Wu, M. Wang, W.-H. Zhang, Y. Lu, S. Yang, S. Yang, Zwitterion coordination induced highly orientational order of $CH_3NH_3PbI_3$ perovskite film delivers a high open circuit voltage exceeding 1.2 V, Adv. Funct. Mater. 29 (2019) 1901026, https://doi.org/10.1002/adfm.201901026.
[62] N. Chen, X. Yi, J. Zhuang, Y. Wei, Y. Zhang, F. Wang, S. Cao, C. Li, J. Wang, An efficient trap passivator for perovskite solar cells: poly(propylene glycol) bis (2-aminopropyl ether), Nano-Micro Lett. 12 (2020) 177, https://doi.org/10.1007/s40820-020-00517-y.
[63] J.-W. Lee, D.-H. Kim, H.-S. Kim, S.-W. Seo, S.M. Cho, N.-G. Park, Formamidinium and cesium hybridization for photo- and moisture-stable perovskite solar cell, Adv. Energy Mater. 5 (2015) 1501310, https://doi.org/10.1002/aenm.201501310.
[64] C. Bi, Q. Wang, Y. Shao, Y. Yuan, Z. Xiao, J. Huang, Non-wetting surface-driven high-aspect-ratio crystalline grain growth for efficient hybrid perovskite solar cells, Nat. Commun. 6 (2015) 7747, https://doi.org/10.1038/ncomms8747.
[65] J. Wang, Z. Gao, J. Yang, M. Lv, H. Chen, D.-J. Xue, X. Meng, S. Yang, Controlling the crystallization kinetics of lead-free tin halide perovskites for high performance green photovoltaics, Adv. Energy Mater. 11 (2021) 2102131, https://doi.org/10.1002/aenm.202102131.
[66] Q. Dong, Y. Fang, Y. Shao, P. Mulligan, J. Qiu, L. Cao, J. Huang, Electron-hole diffusion lengths >175 μm in solution-grown $CH_3NH_3PbI_3$ single crystals, Science 347 (2015) 967–970, https://doi.org/10.1126/science.aaa5760.
[67] V. Sarritzu, N. Sestu, D. Marongiu, X. Chang, S. Masi, A. Rizzo, S. Colella, F. Quochi, M. Saba, A. Mura, G. Bongiovanni, Optical determination of Shockley-Read-Hall and interface recombination currents in hybrid perovskites, Sci. Rep. 7 (2017) 44629, https://doi.org/10.1038/srep44629.
[68] J. Chen, N.-G. Park, Causes and solutions of recombination in perovskite solar cells, Adv. Mater. 31 (2019) 1803019, https://doi.org/10.1002/adma.201803019.
[69] Q. Wang, Y. Shao, H. Xie, L. Lyu, X. Liu, Y. Gao, J. Huang, Qualifying composition dependent p and n self-doping in $CH_3NH_3PbI_3$, Appl. Phys. Lett. 105 (2014) 163508, https://doi.org/10.1063/1.4899051.
[70] D.B. Khadka, Y. Shirai, M. Yanagida, K. Miyano, Degradation of encapsulated perovskite solar cells driven by deep trap states and interfacial deterioration, J. Mater. Chem. C 6 (2018) 162–170, https://doi.org/10.1039/C7TC03733C.